Acta Materialia 307 (2026) 121966

Contents lists available at ScienceDirect

Acta Materialia

journal homepage: www.elsevier.com/locate/actamat

A dual-phase strain-transformable zirconium alloy with exceptional yield strength (1.2 GPa) and low elastic modulus (70 GPa) via TWIP and phase reversion

Junhui Tang [a], Nicolas Jobit [b], Agata Sotniczuk [c], Witold Chromiński [d], Denis Laillé [b], Daniel Galy [e], Philippe Vermaut [a,f], Phillippe Castany [b], Thierry Gloriant [b], Ju Li [g], Frédéric Prima [a], Fan Sun [a,*]

[a] PSL Research University, Chimie ParisTech, CNRS-UMR8247, Institut de Recherche de Chimie Paris, Paris, 75005, France
[b] Institut des Sciences Chimiques de Rennes, UMR CNRS 6226, INSA de Rennes, 20 Avenue des Buttes de Coesmes, F-35043 Rennes Cedex, France
[c] NOMATEN Centre of Excellence, National Centre for Nuclear Research, A. Soltana 7, 05-400 Otwock Świerk, Poland
[d] Warsaw University of Technology, Faculty of Materials Science and Engineering, Woloska 141, 02-507 Warsaw, Poland
[e] SAFRAN Paris Saclay, Magny-les-Hameaux, 78772, France
[f] Sorbonne University, UPMC University Paris, UFR926, Paris, 75005, France
[g] Department of Nuclear Science and Engineering and Department of Materials Science and Engineering, Massachusetts Institute of Technology, Cambridge, MA 02139, USA

ARTICLE INFO

Key words:
BCT+β dual-phase
High strength
Low elastic modulus
TWIP effect
Zr alloys

ABSTRACT

The present study focuses on the development of a novel Zr-12Nb-3Sn alloy displaying a body-centered tetragonal (BCT) / β dual-phase microstructure and engineered to achieve a superior combination of high strength and low elastic modulus. The BCT phase is shown to play a critical role in enhancing strength without increasing elastic modulus. Comprehensive analyses using *in situ* straining electron backscatter diffraction (EBSD) experiment and transmission electron microscopy (TEM) were conducted to characterize the microstructure of the BCT phase and the associated deformation mechanisms, including dislocation slip, stress-induced reversion from BCT to β transformation, and mechanical twinning. The present findings reveal that the BCT phase and mechanical twinning both contribute to material strengthening, whereas the stress-induced reversion of the BCT phase to β acts as a mechanism for stress relaxation. As a result, the alloy demonstrates exceptional mechanical performance, achieving a yield strength exceeding 1200 MPa, an elastic modulus of approximately 70 GPa, and an elongation of ~13%.

1. Introduction

Metallic materials such as stainless steel (SS), Co-Cr alloys, titanium (Ti), and zirconium (Zr) alloys are widely used in biomedical applications, particularly orthopedic implants [1–3]. In recent years, β-type Ti and Zr alloys with non-toxic alloying elements have gained attention as promising alternatives to SS and Co-Cr alloys due to their superior biocompatibility [4]. A significant challenge associated with orthopedic implants is the "stress shielding" effect, which arises due to the mismatch in stiffness between implant materials and native bone, consequently reducing mechanical loading on adjacent bone tissue, disrupting normal bone remodeling processes, and ultimately resulting in bone resorption or osteoporosis [5]. The issue is especially critical in load-bearing implants, where materials with a high elastic modulus absorb excessive stress, further diminishing mechanical stimulation and increasing the risk of implant loosening or refracture after removal. Therefore, selecting materials that combine high strength with a low elastic modulus comparable to that of bone, is essential for long-term implant stability and for reducing the likelihood of revision surgery [3].

In the body-centered cubic (BCC) alloys, β-type Ti alloys exhibit a wide range of mechanical properties depending on their chemical composition. Extensive research has focused on designing novel β-type Ti alloys with low elastic modulus using the semi-empirical "*d*-electron alloy design method" proposed by Morinaga et al. [6–8]. This approach

* Corresponding author.
E-mail address: fan.sun@chimieparistech.psl.eu (F. Sun).

https://doi.org/10.1016/j.actamat.2026.121966
Received 18 September 2025; Received in revised form 6 January 2026; Accepted 24 January 2026
Available online 25 January 2026

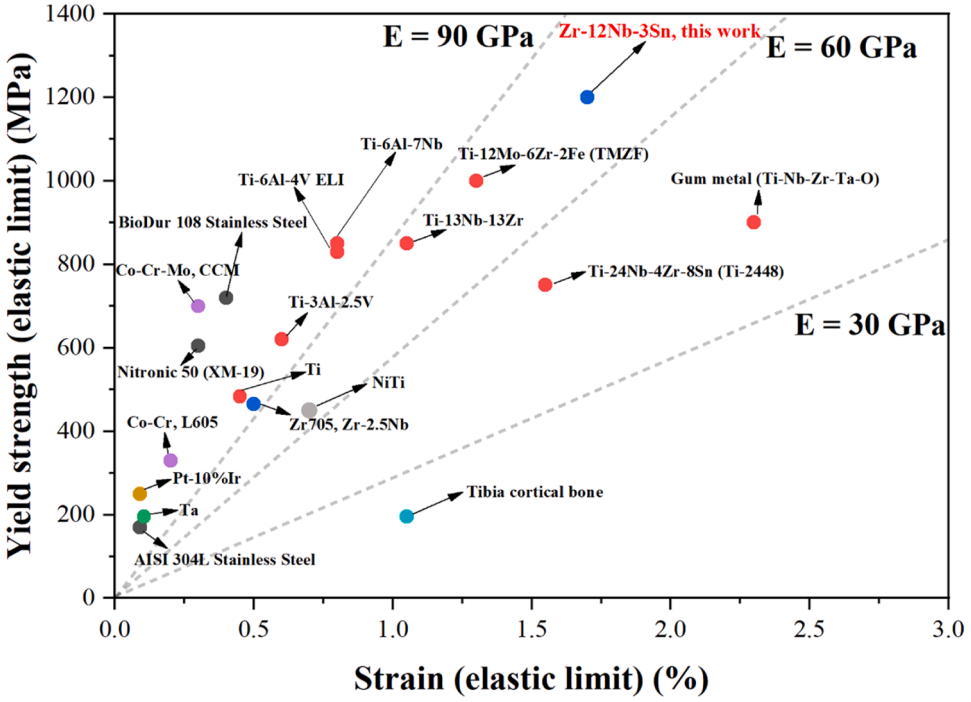

Fig. 1. The yield strength and strain for the bone implant materials. Data source: ANSYS Granta EduPack 2024 [35].

relates two key electronic parameters, B_o (the covalent bonding strength between alloying elements) and M_d (the average d-orbital energy level, reflecting electronegativity and atomic radius), to the chemical stability of the β phase. The resulting $\overline{Bo} - \overline{Md}$ diagram has been used to correlate β phase stability with the primary deformation mechanisms, including dislocation slip, stress-induced martensite (SIM) formation contributing to the shape-memory effect and superelasticity, the transformation-induced plasticity (TRIP) effect, and the mechanical twinning associated with the twinning-induced plasticity (TWIP) effect, supported by experimental evidence from metastable Ti alloys [9–11]. Based on this framework, several single β-phase Ti alloys with low modulus have been developed, including Ti-Zr-Mo [12], Ti-Nb-Zr [13], Ti-Nb-Zr-Sn [14] and Ti-Nb-Ta-Zr series alloys [15–18]. Compared to β-type Ti alloys, β-type Zr alloys exhibit a similar landscape of deformation mechanisms with excellent biocompatibility, high X-ray radio-opacity and low magnetic susceptibility, which allows mechanism-driven biomedical alloy design for desired mechanical performance by combining phase transformation, TRIP/TWIP, high ductility, high strength, and low elastic modulus [19]. In recent years, increasing attention has been directed toward developing β-type Zr alloys that combine low modulus with low magnetic susceptibility for improved biomedical performance [19–24].

Although recent developments in single β-phase Ti and Zr alloys have significantly advanced in the control of the stress-induced phase transformation and mechanical twinning, their yield strength remains inferior to that of conventional α+β dual-phase Ti alloys [25]. To address this limitation, various strategies have been explored, including strengthening TRIP/TWIP-type alloys like Ti-12Mo [26] and Ti-7Cr-1.5Sn [27] through ω_{iso} and α phase precipitations. The ω_{iso} phase offers notable strengthening but is difficult to control during processing to avoid the embrittlement [26,28,29]. The α phase has more complexity in distribution, size and morphology. The grain boundary α precipitates are linked to early intergranular failure, while nanoscale precipitation is a well-known cause of possible embrittlement. Conversely, the well-controlled nucleation and growth of intragranular lath α phases in additively manufactured alloys can enhance strength while preserving SIM and ductility [30], enabling effective shear strain accommodation in the matrix. Beyond ω_{iso} and α phase, a BCT phase has been identified in a dual-phase metastable β Zr-Nb alloys comprising quenched-in BCT phase in BCC matrix [22,31–34]. The BCT phase has been observed to demonstrate significant resistance to deformation relative to the BCC matrix under high stress, indicating a strong potential for alloy strengthening.

In this work, we investigate the deformation mechanism of a BCT-strengthened Zr-12Nb-3Sn alloy designed within the framework of the "Bio-TWIP" Zr alloy concept proposed in previous studies [32]. In this alloy, we pushed the β stability to the maximum before completely suppressing the mechanical twinning, aiming at a high critical resolved shear stress (CRSS) for twinning. This enables the design of a Zr alloy that integrates high strength, low elastic modulus, and TWIP behavior. The present study establishes a proof-of-concept for tunable dual-phase Zr alloys, with comprehensive analysis of the BCT phase microstructure, mechanical performances, deformation mechanisms, and alloy design strategy.

2. Experimental

The Zr-12Nb-3Sn (wt.%) alloy ingot was fabricated by vacuum arc melting of commercially pure Zr, Nb, and Sn metals. The melting process was repeated at least five times in a Buhler AM500 arc furnace under high-purity argon to ensure chemical homogeneity. Post-melting, the ingot was annealed at 1193 K for 30 min in a vacuum tubular furnace at 2.0×10^{-6} Pa, followed by water quenching. Sheets with a final thickness of 0.5 mm were obtained by cold rolling to a 90% reduction in thickness. These were subsequently recrystallized at 1193 K for 30 min under the same vacuum condition, then quenched in water to retain a β-phase matrix (hereafter referred to as the solution treated (ST) state). Tensile specimens with a thickness of 0.5 mm and gauge dimensions of 10×4 mm^2 were machined from the rolled sheets.

Microstructural analyses were conducted using electron backscatter diffraction (EBSD), conventional transmission electron microscopy (TEM), and high-resolution scanning transmission electron microscopy (HRSTEM). EBSD was performed using a ZEISS Merlin FE-SEM at 15 kV equipped with a Bruker-Nano EBSD system. TEM imaging was carried out with a JEOL 2100plus at 200 kV, and HRSTEM analysis was

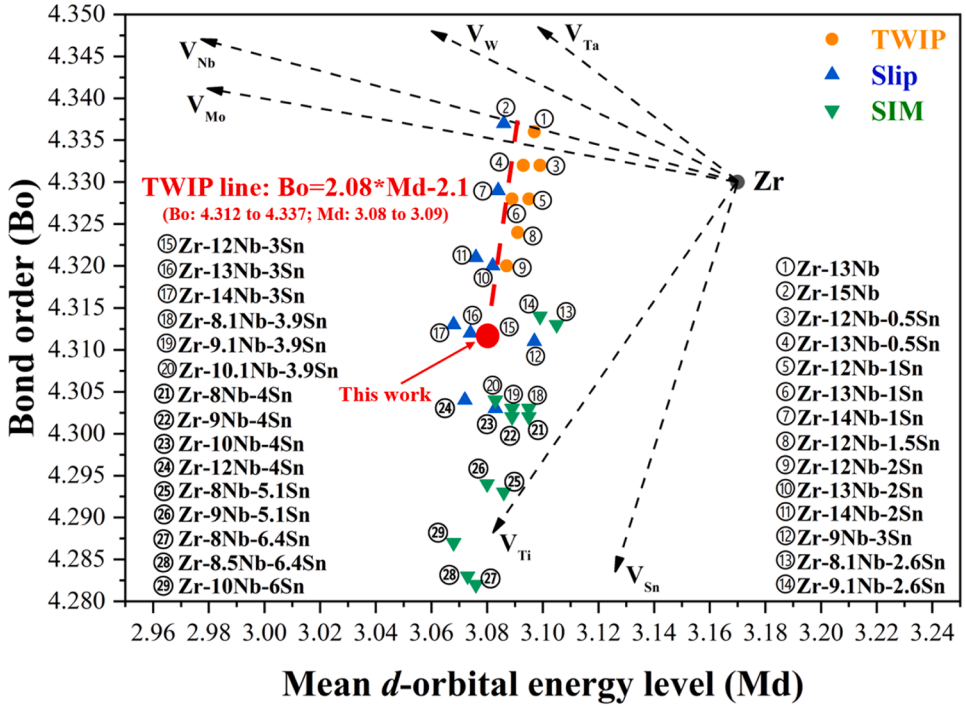

Fig. 2. The d-electron alloying diagram for zirconium alloys, showing alloying vectors of selected elements as functions of B_o and M_d. The red dashed line represents the TWIP line, separating compositions favoring twinning-induced plasticity (TWIP) from those dominated by dislocation slip [32].

performed on a Cs-corrected Thermo Fisher Scientific Spectra 200 STEM-HAADF (detector collection angle 45-200 mrad). Mechanical testing, including uniaxial and cyclic tensile tests, was conducted on an INSTRON 5966 at room temperature with a constant strain rate of 10^{-3} s^{-1}. Microstructural evolution during the early deformation stages was investigated using interrupted straining. After each strain increment, the strain was held to allow stress relaxation while EBSD maps were acquired in the SEM. Nanoindentation was performed using a Nano Hardness Tester (NHT, CSM Instruments) with a Berkovich tip. The tests were conducted in load control mode with a maximum force of 50 mN, and the results were analyzed via the Oliver-Pharr method and presented as instrumented Vickers hardness (HVIT). For EBSD sample preparation, specimens were ground with SiC papers down to 4000 grit, polished using colloidal silica (OPS) in a VibroMet system for 5 to 20 h, and subsequently ion-milled at 8 kV and 4 degrees for 20 min, followed by 4 kV and 4 degrees for 40 min. TEM samples were prepared by twin-jet electropolishing in a solution of 7% sulfuric acid in methanol at -30°C.

3. Alloy design

Fig. 1 presents the yield strength and maximum reversible elastic strain of common metallic materials used in orthopedic implants, derived from the Ashby diagram. Fig. 2 shows the d-electron alloying diagram for zirconium alloys, where alloying vectors of various elements are plotted as functions of B_o and M_d, indicating different deformation mechanisms in potential alloys. A TWIP line, marked by a red dashed line, is drawn on the $\overline{Bo} - \overline{Md}$ diagram to represent the empirical transition between twinning-induced plasticity (TWIP) and dislocation slip. Based on previous observations in the Zr-Nb-Sn system [32], TWIP behavior occurs on the right side of this line, while classical dislocation slip dominates on the left. The objective of this study is to develop a Zr-based alloy with high strength, low modulus, and twinning-induced plasticity for load-bearing orthopedic implants. The key strategy for achieving high strength is to maximize β-phase stability without entirely suppressing the TWIP effect. This approach ensures that the alloy benefits from a high yield stress due to the elevated triggering stress required for mechanical twinning. Although twinning-induced strain hardening is more limited compared to alloys with a lower triggering stress, it plays a crucial role in stabilizing plastic flow. This strategy enables a balance in which stress is maximized while preserving sufficient mechanical twinning to prevent strain localization, a critical safety concern for permanent implants. Meanwhile, the addition of Sn to binary Zr-Nb alloys promotes solid solution strengthening and improves cold workability. Sn is also known to suppress ω phase formation in metastable BCC alloys, a trend similarly observed in the Zr-Nb-Sn system. However, to ensure precipitation of the ω_{ath} phase, the Sn content was deliberately limited to approximately 3 wt.%. Exceeding this content results in the near disappearance of the ω phase in solution-treated conditions, thereby limiting its ability to serve as a precursor for subsequent strengthening mechanisms [32]. Accordingly, the composition point was selected as indicated in Fig. 2. As illustrated here, the present alloy design follows a straightforward methodology based on $\overline{Bo} - \overline{Md}$ mapping developed for biomedical Zr alloys, with the optimal composition positioned along the TWIP line and near the TWIP limit to maximize yield strength while satisfying the design criteria.

4. Results

4.1. BCT + β dual phase structure after quenching

The BCT phase was first identified in 1957's annual progress report of Oak Ridge National Laboratory as a martensitic Widmanstätten structure in β-quenched Zr-Nb alloys [36], and subsequent studies suggested more complex crystallographic possibilities [37]. Recent investigations have reported similar BCT structures in β-type Zr-Nb-Sn alloys produced via laser-based additive manufacturing and conventional quenching methods, noting reversible transformations and defined crystallographic relationships [34]. A Zr-Hf-rich BCT phase with three inequivalent variants has also been identified in HfNbTaTiZr high-entropy alloy [38]. Despite these findings, key aspects such as mechanical contributions, and stress-induced stability remain unclear.

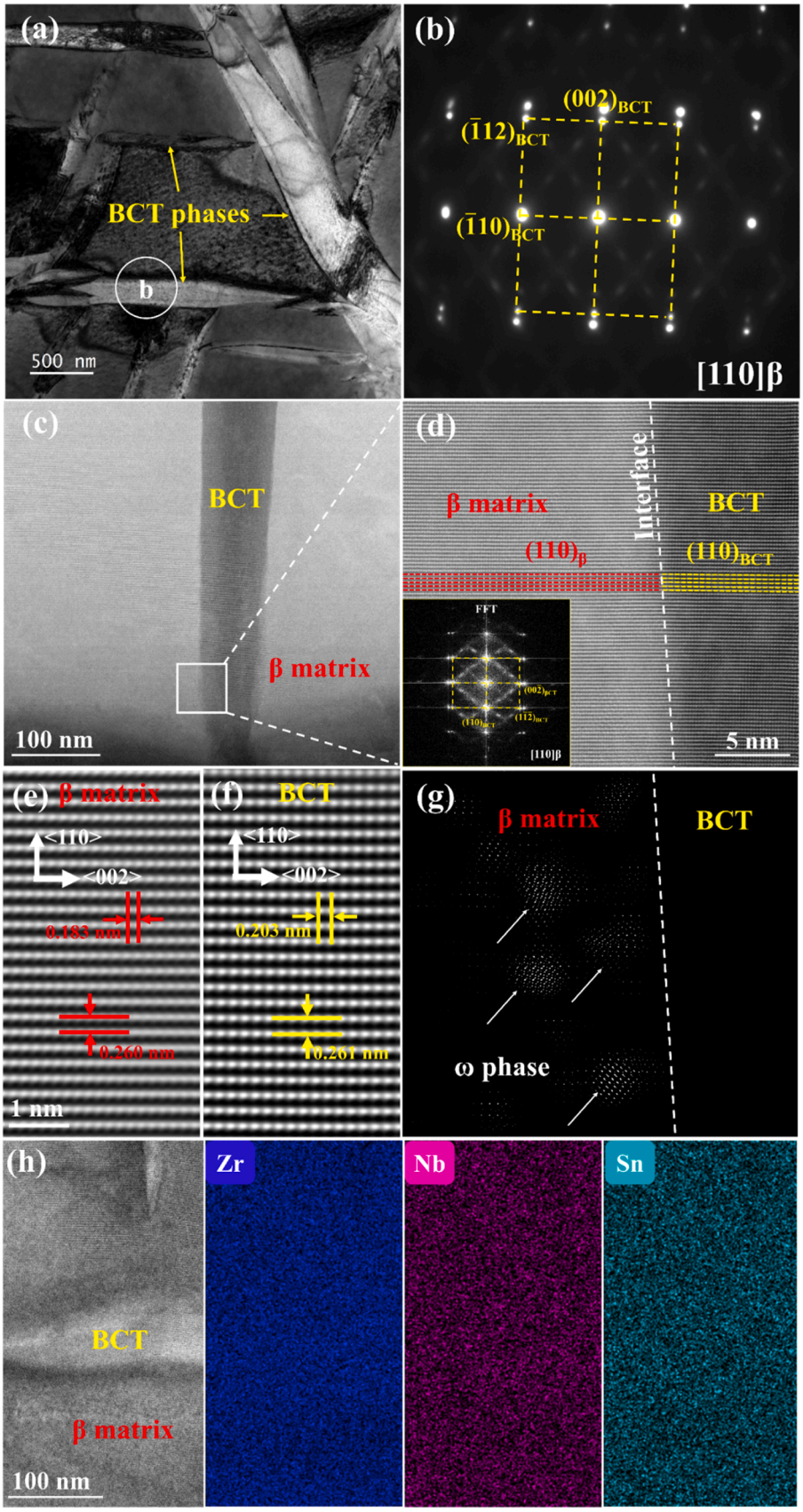

(caption on next page)

Fig. 3. TEM and high-resolution (HR) TEM micrographs of the Zr-12Nb-3Sn sample at ST state. (a) Bright-field (BF) image illustrating the β + BCT dual phase structure; (b) selected area electron diffraction (SAED) patterns corresponding to the regions marked in (a); (c) HAADF-STEM image showing the β matrix and BCT phase; (d) HAADF-HRSTEM image of the selected area marked in (c), highlighting the BCT/β interface (delineated by a white dashed line). The inset shows the corresponding Fourier transform (FFT), with the interface corresponding to the (110) plane for both the BCT and β phases; (e) and (f) Inverse Fourier transform (IFFT) images providing close-ups of the β matrix and BCT phase, respectively; (g) IFFT image showing the distribution of ω_{ath} phases, which are exclusively found in the β matrix; (h) BF image showing the β + BCT dual phase structure and corresponding elemental distributions of Zr, Nb, and Sn.

This study provides a comprehensive examination of the BCT phase, addressing these unresolved issues through detailed structural and mechanical analyses.

TEM observations of the Zr-12Nb-3Sn sample at ST state along $<110>_\beta$ zone axis are shown in Fig. 3. In Fig. 3a, the BCT in bright-field (BF) image was observed in lenticular shape with thickness approximately 100 nm, consistent with EBSD results in Fig. 4. The selected area electron diffraction (SAED) pattern recorded along $<110>_\beta$ zone axis in Fig. 3a demonstrates the lattice correspondence between BCT and parent β phase: $[110]_{BCT}$ // $[110]_\beta$, $(002)_{BCT}$ // $(002)_\beta$, $(1\bar{1}0)_{BCT}$ // $(1\bar{1}0)_\beta$; $d_{1\bar{1}0BCT} = d_{1\bar{1}0\beta}$; $d_{002BCT} = 1.1d_{002\beta}$, consistent with previous studies in Zr-13Nb [31] and HfNbTaTiZr high-entropy alloys [38]. Additionally, the SAED pattern of the β matrix displays superlattice reflections at 1/3 and 2/3 $\{112\}_\beta$ positions, indicating the presence of the ω_{ath} phase formed during water quenching [39]. STEM was employed to analyze the nanoscale interface between the BCT and β phases. As shown in Fig. 3d, which provides a magnified view of the BCT region indicated in Fig. 3c, the interface is well-defined, indicating that the BCT phase is a stable constituent within the β matrix. No transition zone was detected at the interface, suggesting a fully coherent relationship between the BCT and β phases. Moreover, no geometrically necessary dislocations (GNDs) or stacking faults were observed within the coherent interface region. However, significant lattice misfit occurs at the edge of the BCT plates, explaining their observed lenticular morphology. The Fast Fourier transform (FFT) inset in Fig. 3d shows diffraction features consistent with the conventional TEM pattern in Fig. 3b. Figs. 3e and 3f display inverse FFT (IFFT) images highlighting the β matrix and BCT phase, respectively. The measured interplanar spacings for the β phase are 0.260 nm for {110} and 0.183 nm for {002}, while for the BCT phase they are 0.261 nm and 0.203 nm, respectively. These measurements further confirm the lattice correspondence observed in the conventional TEM analysis. Finally, the IFFT image in Fig. 3g has revealed the morphology and distribution of ω_{ath} phase in the β matrix, after the quenching stage. Moreover, no discernible compositional difference between the β matrix and the BCT phase is observed in the elemental distributions shown in Fig. 3h.

Fig. 4 shows EBSD analyses of the Zr-12Nb-3Sn alloy at ST state. The band contrast (BC) map and inverse pole figure (IPF) map in Fig. 4a reveal a dual-phase microstructure consisting of equiaxed recrystallized β grains with a high density of embedded BCT phase. This dual-phase morphology is further confirmed by the BC + phase map shown in Fig. 4b, where the β and BCT phases are clearly distinguished on the basis of symmetry in Kikuchi patterns. The BCT phase exhibits an acicular morphology at the sample surface, consistent with previous reports [31,32,34]. In order to clarify whether the BCT phase adopts an acicular or plate-like morphology within the alloy volume, which is essential for understanding its contribution to deformation behavior, morphological analysis was performed by examining BCT features projected on β grains with surface normal close to the $(100)_\beta$, $(110)_\beta$ and $(111)_\beta$ planes. The plate-like morphology is confirmed, as shown in Fig. 4a-d. In certain β grains oriented near [001], the BCT lamellae cover the β grains, as clearly observed through EBSD indexing in Fig. 4b.

The BCT phase forms through unidirectional lattice dilatation of the parent β phase, resulting in three distinct crystallographic variants based on the direction of dilation.

BCT Variant 1 (BCT V1) arises from dilation along the $[100]_\beta$ direction, leading to an increase in the a-axis spacing while the b- and c-axes of the β phase remain unchanged.

Similarly, BCT Variant 2 (BCT V2) and Variant 3 (BCT V3) are formed through dilation along the *b*- and *c*-axes of the β phase, respectively.

The surface morphologies of these three variants, along with their projections onto different crystallographic planes of the β matrix, are illustrated schematically and experimentally through EBSD analysis in Fig. 4b-d. Fig. 4b presents a schematic representation and corresponding EBSD BC + IPF map and BC + Phase map of a β grain with a $[100]_\beta$ surface normal. According to the BC + IPF map, BCT V1 is oriented perpendicular to BCT V2, whereas BCT V3 variants, whose plate normals are aligned with the $[100]_\beta$ direction, appear to cover the entire grain surface. Fig. 4c shows the schematic and EBSD results for a grain with a $[110]_\beta$ surface normal. In this orientation, BCT V1 and V2 are aligned parallel to each other and are both oriented perpendicular to BCT V3. Fig. 4d includes the corresponding data for a grain oriented along $[111]_\beta$. In this case, the three BCT variants are sectioned by a plane inclined at approximately 45 degrees to the principal axes, with each variant forming an angle of approximately 60 degrees with respect to the others. The crystallographic orientation relationships between the β and BCT phases are further confirmed by pole figure analysis of a grain near the $(111)_\beta$ orientation, as shown in Fig. 4e.

To investigate the mechanical properties of the BCT phase, nanoindentation experiments were performed on the Zr-12Nb-3Sn sample at ST state, as shown in Fig. 5, to compare the nano-hardness of the BCT phase with that of the β matrix. The results indicate that the hardness of the BCT phase ([2]: 197.7 HVIT) is comparable to that of the β phase ([1]: 201.8 HVIT and [3]: 197.1 HVIT), suggesting that the BCT phase does not exhibit significantly higher intrinsic hardness than the β phase. Furthermore, the elastic modulus of the BCT phase is also similar to that of the β matrix. This behavior is beneficial for biomedical applications, as it prevents a substantial increase in the overall modulus of the alloy, unlike strengthening mechanisms involving high-modulus phases such as α and ω_{iso}.

4.2. Tensile behavior

The uniaxial tensile loading curve of the solution-treated Zr-12Nb-3Sn specimen is shown in Fig. 6. The engineering stress-strain curve in Fig. 6a exhibits a low elastic modulus (70 GPa) and superior yield strength (YS) of over 1200 MPa while maintaining ~13% elongation. The linear elasticity observed in the unloading stress-strain curve at 5% suggests that no reversible deformation mechanisms are likely operational in the alloy during unloading. The inset of Fig. 6b shows strain-hardening rate evolution as a function of true strain. The strain-hardening rate of Zr-12Nb-3Sn is observed to decrease from very high rates due to elastic-plastic transition until the formation of necking where $d\sigma / d\varepsilon = \sigma$ (Considère line shown in dashed line in the inset of Fig. 6b). The strain-hardening rate of Zr-12Nb-3Sn alloy stays above the Considère line until ~1400 MPa, showing a uniform elongation of 11%.

4.3. Strain-induced reversion of BCT to β characterized by EBSD and TEM observations

In situ EBSD mapping was performed on specimens strained to different levels to investigate the evolution of the microstructure. Fig. 7a-d show EBSD analyses from the same region of the Zr-12Nb-3Sn sample at varying strain levels. Three variants of the BCT phase can be indexed in Fig. 7a and 7b. After 5% deformation followed by unloading,

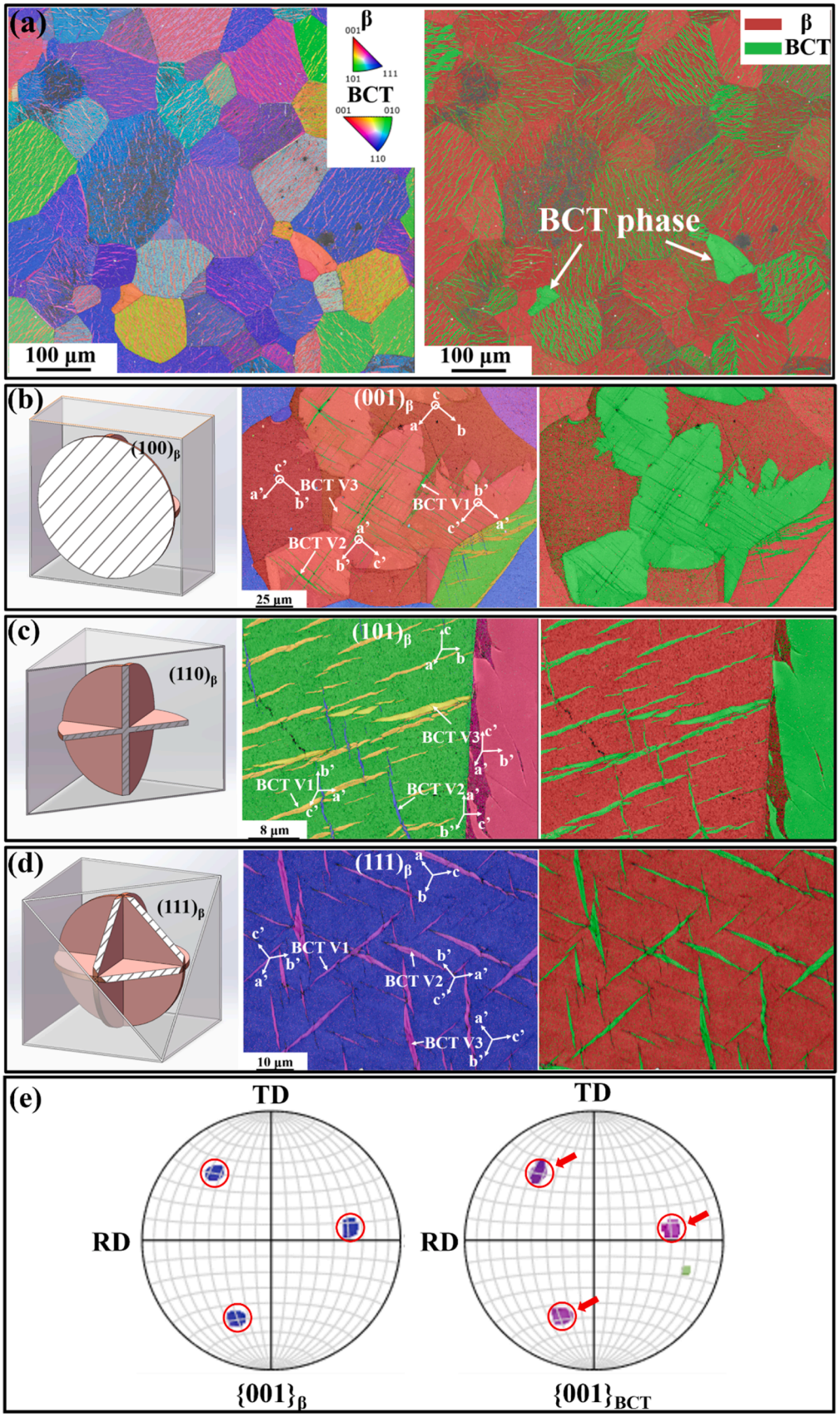

Fig. 4. Microstructural characterizations of Zr-12Nb-3Sn sample at ST state. (a) EBSD Band Contrast (BC) + Inverse Pole Figure (IPF) map, along with BC + Phase map; (b-d) Schematic diagrams illustrating the morphologies of BCT phases on the $(100)_\beta$, $(110)_\beta$ and $(111)_\beta$ planes, respectively, accompanied by EBSD BC + IPF map and BC + Phase map; the unit cell orientation is indexed on the maps. (e) Pole figures of the β and BCT phases.

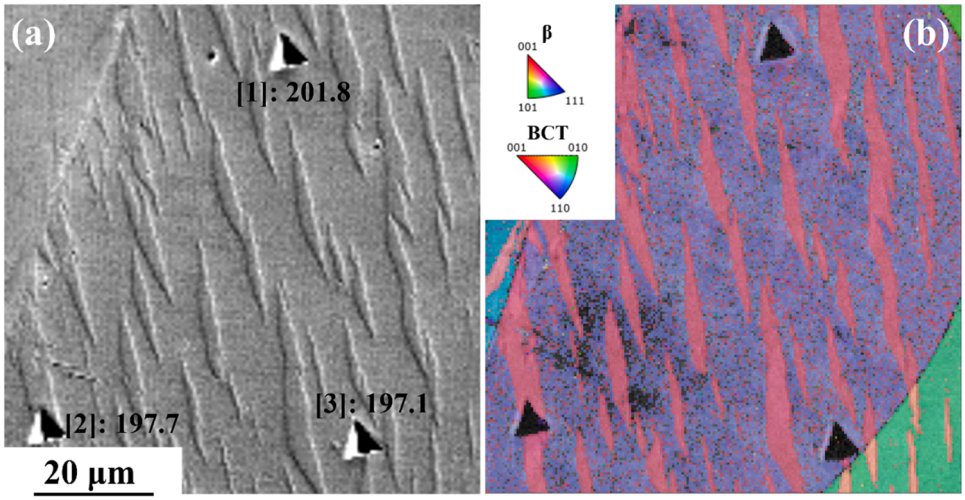

Fig. 5. Nanoindentation of the Zr-12Nb-3Sn sample at ST state. (a) SEM image showing the nanoindentation locations along with the corresponding hardness values; (b) the corresponding EBSD (BC + IPF map) diagram.

Fig. 7d reveals that a portion of the fine BCT phases transformed back into the matrix β phase, as evidenced by the BC + IPF map and BC + Phase map. Higher-magnification examination of a transformed BCT plate (shown in Fig. 7b and 7d) reveals a distinct misorientation of approximately 2°, as demonstrated in the inset of Fig. 7d, between the β phase transformed from the BCT phase (hereafter referred to as 'reverted BCT') and the parent β matrix. This misorientation is indicated by yellow arrows in the BC + IPF map in Fig. 7d and further confirmed by the corresponding misorientation angle profiles shown in the inset of the BC + Phase map. After fracture, mechanical twin bands are observed in the β matrix, as shown in Fig. 7e. Based on the stereographic projection analysis in Fig. 7f, the twinning elements are identified as {332}<113> type β twins, consistent with their orientation relationship with the β matrix. This confirms that the TWIP effect is active through the formation of classical 332T during the plastic deformation. It should be noted that mechanical twinning in this alloy requires a very high critical stress (~1200 MPa), consistent with the alloy design. Typically, mechanical twinning requiring such a high critical stress does not occur in TWIP Ti alloys, due to earlier yielding by dislocation slip at lower stresses [26, 40]. Moreover, most of the BCT phases have transformed back into the β matrix, with the remaining BCT phases appearing only in grains oriented near $(100)_\beta$, where fragments of superficial BCT plates persist on the surface.

To further investigate the stress-induced phase transformation behavior of the BCT phase, TEM analyses were conducted on the fractured Zr-12Nb-3Sn specimen. Fig. 8a presents a BF image revealing regions of reverted BCT within the β matrix. The previously observed 2° misorientation detected by EBSD is not clearly discernible in the SAED pattern shown in Fig. 8b, as such subtle angular deviations are difficult to resolve using TEM diffraction techniques. However, Fig. 8a clearly exhibits a distinct contrast between the reverted BCT and the surrounding β matrix. The SAED patterns, with relevant diffraction spots highlighted in Fig. 8b, confirm the structural transformation of the BCT phase back to the β phase.

Taken together, the combined findings from EBSD and TEM analyses provide direct evidence for the stress-induced transformation of the BCT phase into the β matrix during mechanical deformation.

Fig. 9 presents TEM characterization of mechanical twins formed during deformation. In Fig. 9a, a bright-field image of the fractured Zr-12Nb-3Sn sample shows a mechanical twin within the β matrix. SAED patterns from the twin-matrix interface, the matrix, and the twin (Fig. 9b-d) confirm the crystallographic relationship, further illustrated by the stereographic projection in Fig. 9e, consistent with EBSD observations in Fig. 7e and identifying the twins as 332T [10].

Detailed TEM analyses were carried out to investigate the interaction between the BCT phase and dislocation slip. Fig. 10 presents TEM micrographs of the Zr-12Nb-3Sn sample at the early stage of deformation. The BF image taken along $<111>_\beta$ zone axis in Fig. 10a demonstrates a high density of dislocation slip lines generated in the matrix β phase during the deformation process. Fig. 10b-d exhibit the dislocation slip lines under three g conditions around $<111>_\beta$ zone axis. Dislocation slip lines are observed to be stopped at the BCT phase boundaries, highlighting the strong barrier effect of the BCT phase on dislocations. Fig. 11 demonstrates TEM micrographs of the Zr-12Nb-3Sn sample after fracture. Fig. 11a presents a BF image captured around the $<111>_\beta$ zone axis to visualize the complexity of dislocation patterns. However, the reverted BCT with residual contrast (~2° misorientation to the β matrix) is clearly observed. In contrast, Fig. 11b shows the same region tilted to a two-beams condition, where dislocation patterns not related to the most active system (as marked in Fig. 10a) are clearly distinguishable. This system clearly appears in images taken with other two-beams conditions (Fig. 10c and d) indicating that it features a set of single Burgers dislocations. Notably, dislocation can still be observed to be stopped at the boundaries of the reverted BCT, indicating that these phases continue to act as barriers to dislocation slip lines due to the ~2° misorientation and the presence of GNDs formed to accommodate the volume change associated with the phase transformation.

5. Discussion

The Zr-12Nb-3Sn alloy exhibits a combination of high strength and low elastic modulus, attributed to multiple deformation mechanisms. To elucidate the underlying deformation behavior, several complementary characterization techniques were employed. Three primary deformation mechanisms were identified: dislocation slip, stress-induced reversion of the quenched-in BCT phase, and mechanical twinning. The interaction among these mechanisms results in complex microstructural evolution, which is evident even at early deformation stages.

5.1. BCT's role in the deformation mechanism

The BCT phase in the Zr-12Nb-3Sn alloy, although reported previously, has remained poorly understood in terms of its mechanical properties and role as a secondary plate-like phase in metastable Zr alloys. Our findings reveal that this phase is mechanically unstable and undergoes stress-induced reversion to the parent β phase. The metastability of the BCT has been reported in Zr-9Nb-4Sn alloy [34] showing phase reversion under heating. Nanoindentation results indicate no

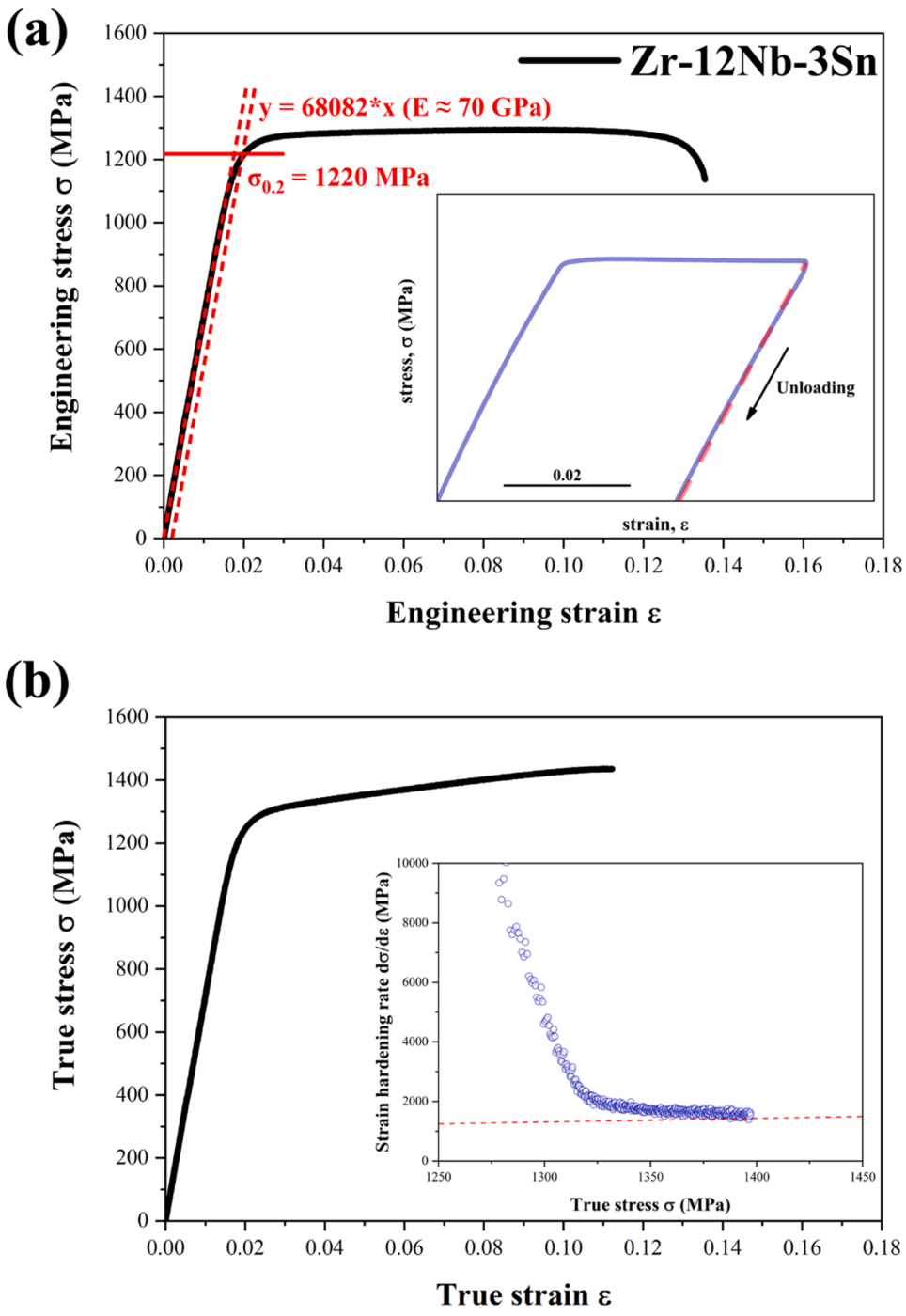

Fig. 6. Mechanical response of the Zr-12Nb-3Sn sample at ST state. (a) Tensile engineering stress-strain curve, the inset is cyclic tensile stress-strain curve; (b) true stress-true strain curve, the inset is the corresponding strain-hardening rate curve as a function of true stress.

significant intrinsic hardness contrast between the BCT and β phases. Due to its unique combination of instability and mechanical parity with the matrix, the BCT phase interacts intricately with applied stress and other deformation mechanisms, contributing to the alloy's ability to achieve high yield strength, low elastic modulus, and decent uniform ductility.

The remarkable combination of strength and ductility investigated in the Zr-12Nb-3Sn alloy can be explained by a multi-stage deformation mechanism. In the initial stage, the interaction between dislocations and as-quenched metastable BCT phases provides a strong strengthening effect, which may be described within a framework analogous to the Hall-Petch relationship in two-phase systems, where the average statistical distance between dislocation sources and obstacles governs strengthening. This is subsequently followed by a TRIP-assisted yielding process, which further enhances ductility without sacrificing strength.

Upon loading, dislocations are generated in the BCC matrix glide until they are arrested by the BCT phases. A key finding of this study is that the BCT phase exhibits a hardness comparable to that of the BCC matrix, as shown in Fig. 5. Thus, the significant strengthening observed cannot be attributed to the BCT phases being intrinsically harder. Instead, the BCT phases act as potent barriers to dislocation motion due to the crystallographic character of the BCC/BCT interface, as presented in Fig. 10. The large tetragonal distortion (~10%) across the interface introduces significant structural and orientational incompatibilities,

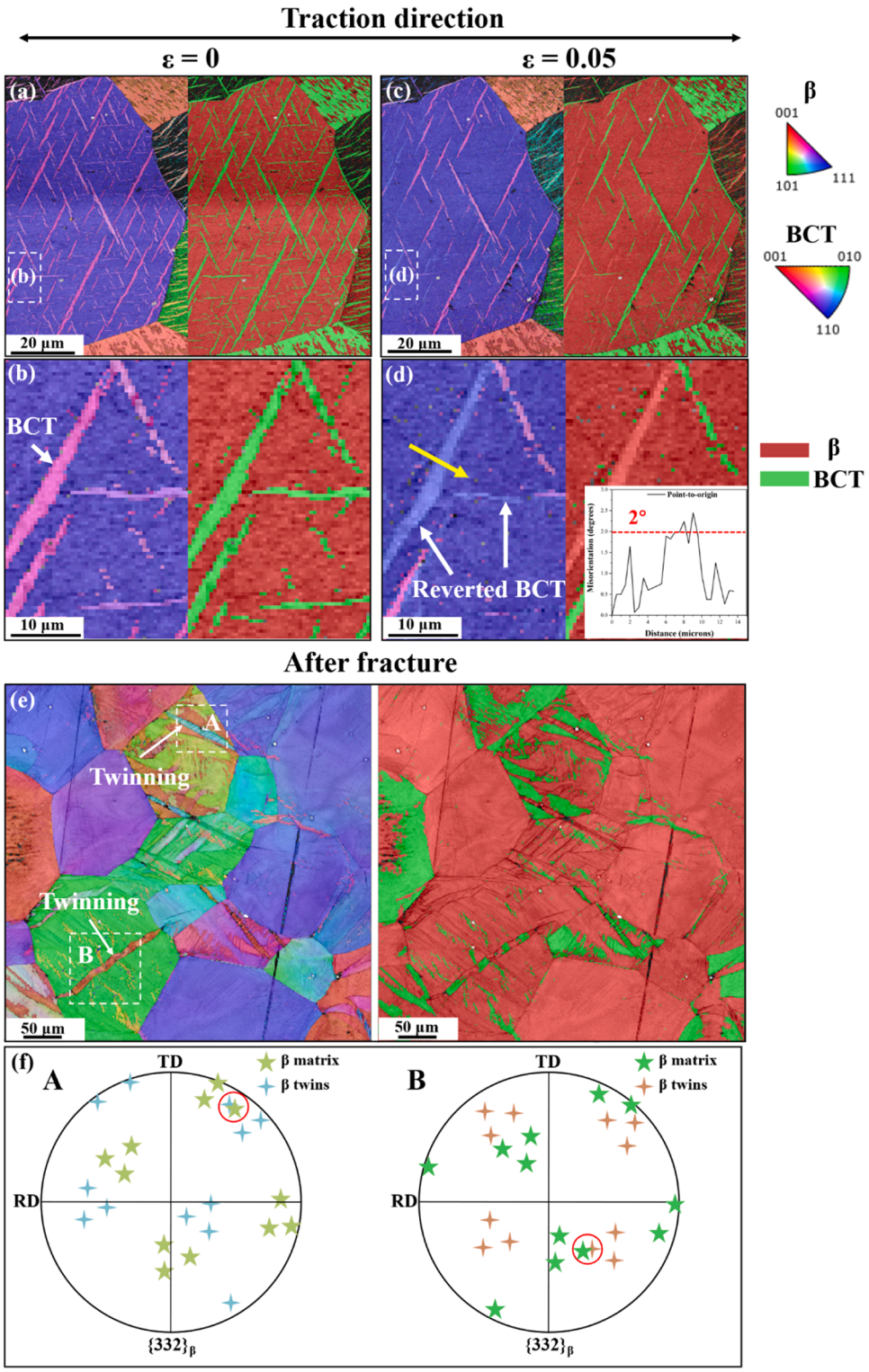

Fig. 7. EBSD (BC + IPF map, BC + Phase map) diagrams of Zr-12Nb-3Sn sample (a-d) during traction taken from the same region: (a) strain ε = 0; (c) strain ε = 0.05 (unloaded state); (b) and (d) close-up images of selected areas in (a) and (c), the inset in (d) is the misorientation angle measured between reverted BCT and matrix β phases with yellow arrows in BC + IPF map of (d); (e) after fracture; (f) stereo projection showing the {332}<113> twin relationship marked in (e).

which hinder the transmission of slip from the matrix into the BCT phase. Consequently, dislocations accumulate at the interface, leading to stress concentration at the pile-up front. This mechanism is directly analogous to that in dual-phase steels [41], where the yield strength is governed by the effective mean free path (d_f) between dispersed secondary phases in the surrounding matrix. Within a Hall-Petch framework, the yield strength can thus be expressed as:

$$\sigma_y = \sigma_0 + k_y d_f^{-1/2}$$

where σ_0 is the friction stress and k_y is the Hall-Petch slope.

In the present case, the distribution of the three crystallographic variants of BCT phases substantially reduces d_f. Furthermore, the

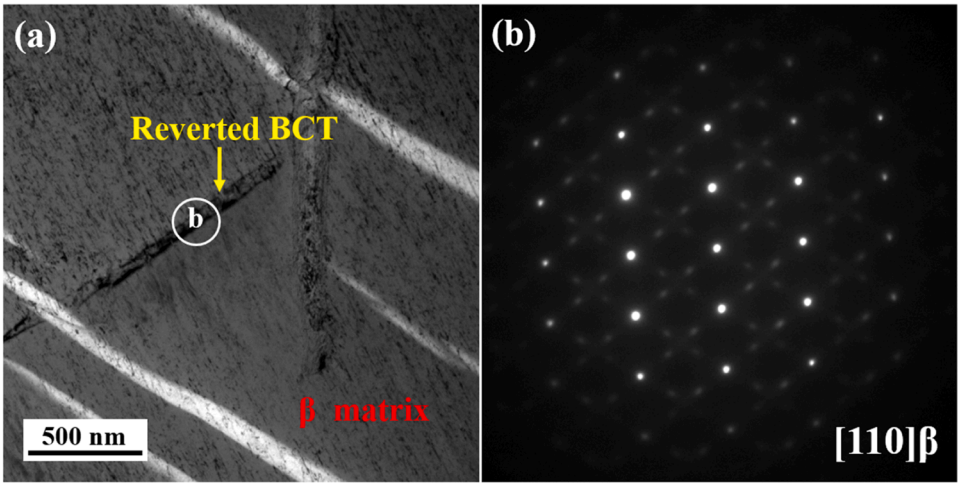

Fig. 8. TEM micrographs of Zr-12Nb-3Sn sample at fracture state. (a) BF image showing β matrix and reverted BCT; (b) corresponding SAED patterns marked in the (a).

secondary phase acts as a highly effective barrier, leading to a pronounced increase in k_y, which reflects barrier strength, with increasing BCT phase volume fraction. A quantitative parallel can be drawn from the work of Chang and Pretan on dual-phase steels [41]: as the volume fraction of secondary phase increases from 0 to 35%, k_y increases by a factor of ~2.1 (from 573.4 to 1209.4 MPa·$\mu m^{1/2}$). In our alloy, where the BCT phase constitutes 10-30 vol.%, a similar effect is anticipated, suggesting that even moderate fractions of a crystallographically distinct second phase can significantly enhance boundary strengthening efficiency. Both the reduction in d_f and the increase in k_y contribute additively to the yield stress, resulting in a two-fold Hall-Petch strengthening effect. This mechanistic framework is consistent with our observations that the yield strength of the Zr-12Nb-3Sn alloy far exceeds that of metastable TWIP-enabled BCC Ti alloys lacking BCT phases.

Consequently, dislocations pile up at their interfaces, leading to significant stress concentrations at the pile-up tip (τ_{tip}), as described by the Eshelby, Frank and Nabarro Eshelby et al. ($\tau_{tip} \approx n \cdot \tau_{applied}$) [42]. Since the number of dislocations in a pile-up (n) is naturally limited by the reduced d_y, a higher applied stress is required to reach the critical stress at the pile-up tip necessary to shear the BCT phase. The tensile results therefore suggest that high local stresses are developed at these pile-ups, ultimately triggering macroscopic yielding. Unlike the cases of α' or α'' in BCC systems, no evidence of reorientation or mechanical twinning is observed in the BCT phases. Instead of yielding through dislocation penetration of the precipitates, as reported for α or ω phases [15], our observations indicate a TRIP-assisted mechanism: the stress concentration at the pile-up tip is sufficient to induce a reverse transformation of the metastable BCT phases into the stable BCC structure.

This phase reversion effectively eliminates the primary barrier to dislocation motion. The local stress required to trigger the transformation is reflected macroscopically as the high yield strength of the alloy, which exceeds that of TWIP Ti alloys where grain boundaries are the sole strengthening obstacles, as illustrated in Fig. 12. The newly formed BCC regions exhibit only a slight misorientation (~2°) relative to the parent matrix, presenting a weak barrier compared to the original high-misfit BCC/BCT interface. Once these phase transformations occur, dislocations propagate more readily across the reoriented regions, facilitating long-range slip and the onset of bulk plastic flow. The progressive and distributed occurrence of these transformation events across the microstructure provides a mechanistic basis for the smooth and continuous yielding behavior observed.

Beyond yielding, plastic stability appears to be sustained by additional mechanisms. The occurrence of 332T at elevated stresses introduces fresh internal interfaces. Although the contribution of the TWIP effect is less pronounced than in classical TWIP alloys [10,31], it likely provides a modest work-hardening effect that delays strain localization and mitigates premature failure.

Altogether, the TRIP-assisted mechanism provides a lower-energy path for strain accommodation by avoiding the need for dislocations to cut through the high-misfit precipitates, a process that is energetically costly and prone to fracture. As a result, the alloy gains strength from the barrier effect of the BCT phases, while ductility is maintained through local stress-induced transformation. Together with the secondary contribution of 332T, this combination of mechanisms explains the observed balance of high strength and good ductility.

5.2. *Mechanism-driven alloy design strategy in metastable Zr-Nb system*

Achieving a combination of high yield strength, low elastic modulus, and high damage tolerance under mechanical overload is a key design objective for such applications. However, these properties are often mutually exclusive, as high strength typically correlates with high modulus and reduced ductility. From an alloy design perspective, leveraging the strengthening effect of secondary phases alongside TWIP effect with high CRSS offers a viable pathway. As shown in TWIP/TRIP Ti systems, such combination is feasible with excellent proof-of-the-concepts [26,27,43]. For β metastable Zr alloys, a similar strategy can be applied to put alloy composition approaching the TWIP line in the $\overline{Bo} - \overline{Md}$ design map (Fig. 2), aiming to maximize the mechanical twinning CRSS which delays the formation of twin at a high stress level to gain higher yielding stress. Meanwhile, BCT plates act as effective strengthening features by interacting with applied stress, dislocation slip, and mechanical twinning. During deformation, the interaction of dislocations with both retained and reverted BCT further contributes to hardening. The activation of mechanical twinning after yielding plays a critical role in preventing strain softening, ensuring the alloy maintains high strength and ductility essential for reliable performance in safety-critical biomedical applications.

The deformation-induced reversion of the BCT phase offers a promising strategy to strengthen TWIP BCC alloys while overcoming the limitations of non-reversible secondary phases such as ω_{iso} and α precipitates. In classic TWIP BCC alloys like Ti-12Mo, ω_{iso} precipitates can raise the yield strength to ~1000 MPa [26], but only within a narrow temperature-time window that controls the precipitate's shear modulus, composition, size, and density. Outside this window, such as at higher aging temperatures or prolonged times, ω_{iso} severely inhibits dislocation slip and mechanical twinning, causing embrittlement through local stress concentration. Moreover, the precipitation of ω_{iso} and α phases are

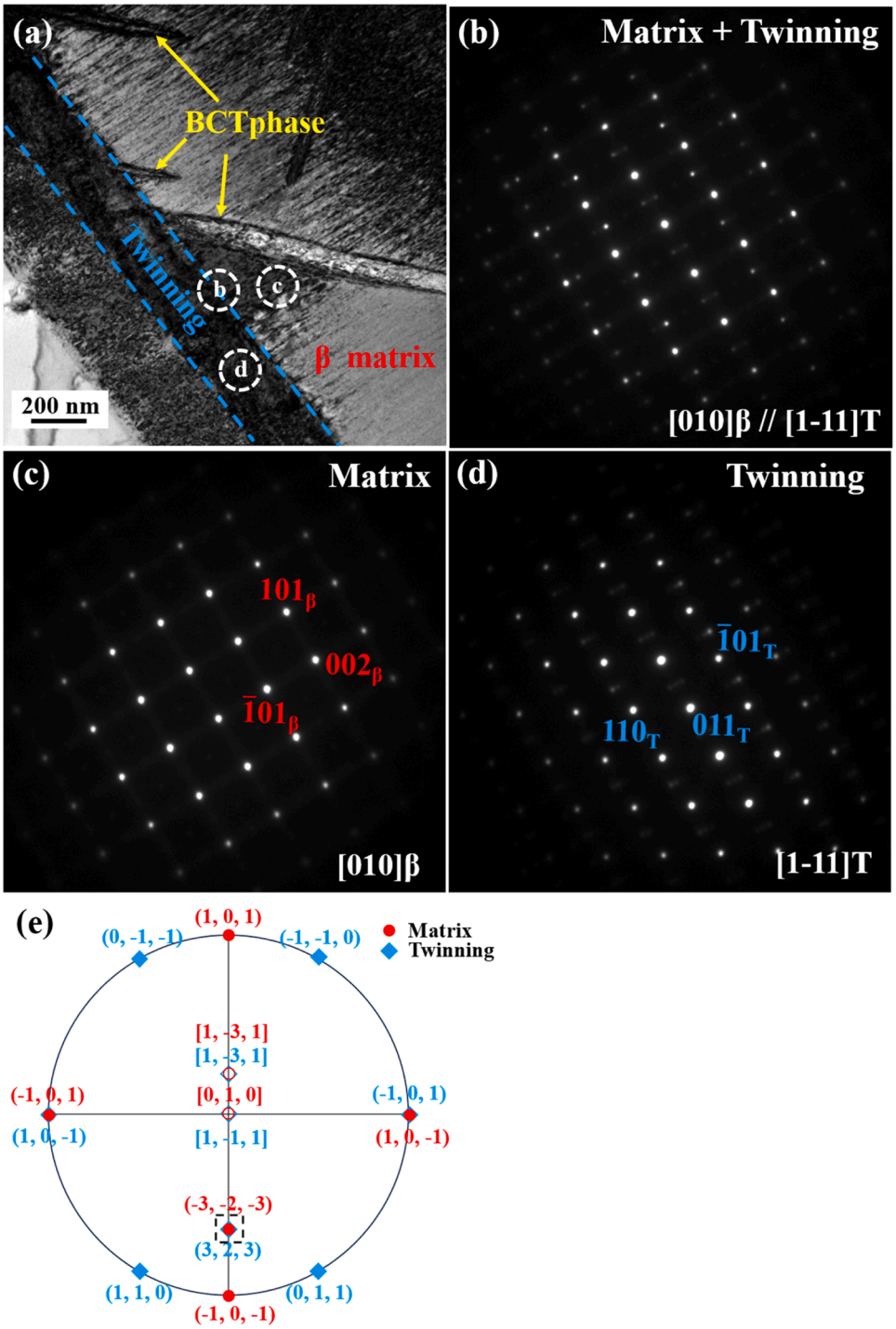

Fig. 9. TEM images of deformation twin. (a) BF image demonstrating interaction between BCT and twin; (b-d) corresponding SAED patterns marked in (a); (e) a schematic stereo projection figure to illustrate the crystallographic relationship of internal 332T layers along the zone axis [010]//[1-11]$_\beta$.

diffusion-controlled processes, leading to local compositional changes in the β matrix and increasing the chemical stability, which suppresses phase transformation and mechanical twinning. In contrast, the BCT phase reverts into β only under relatively high stress, delaying massive dislocation slip and increasing the yield point. Acting analogously to a stress-activated switch, BCT remains inactive at low stress but transforms back into the β matrix upon reaching a critical threshold. This transformation triggers the onset and propagation of dislocation glide and deformation twinning, leading to enhanced yield strength without compromising ductility. Since the hardness values of BCT and β phases are comparable (Fig. 5) and given the positive correlation between hardness and elastic modulus, the BCT phase does not significantly stiffen the alloy, unlike high-modulus precipitates such as ω_{iso} and α [44–46].

Theoretical analysis further highlights the geometrical effect of plate-like precipitates compared to other shapes, such as spherical or cylindrical forms, in precipitation hardening. According to the work of F.R.N. Nabarro [47], thin plate-like precipitates are particularly effective due to their ability to significantly reduce strain energy, consistent with the observation that the BCT phase exhibits a 10% volume

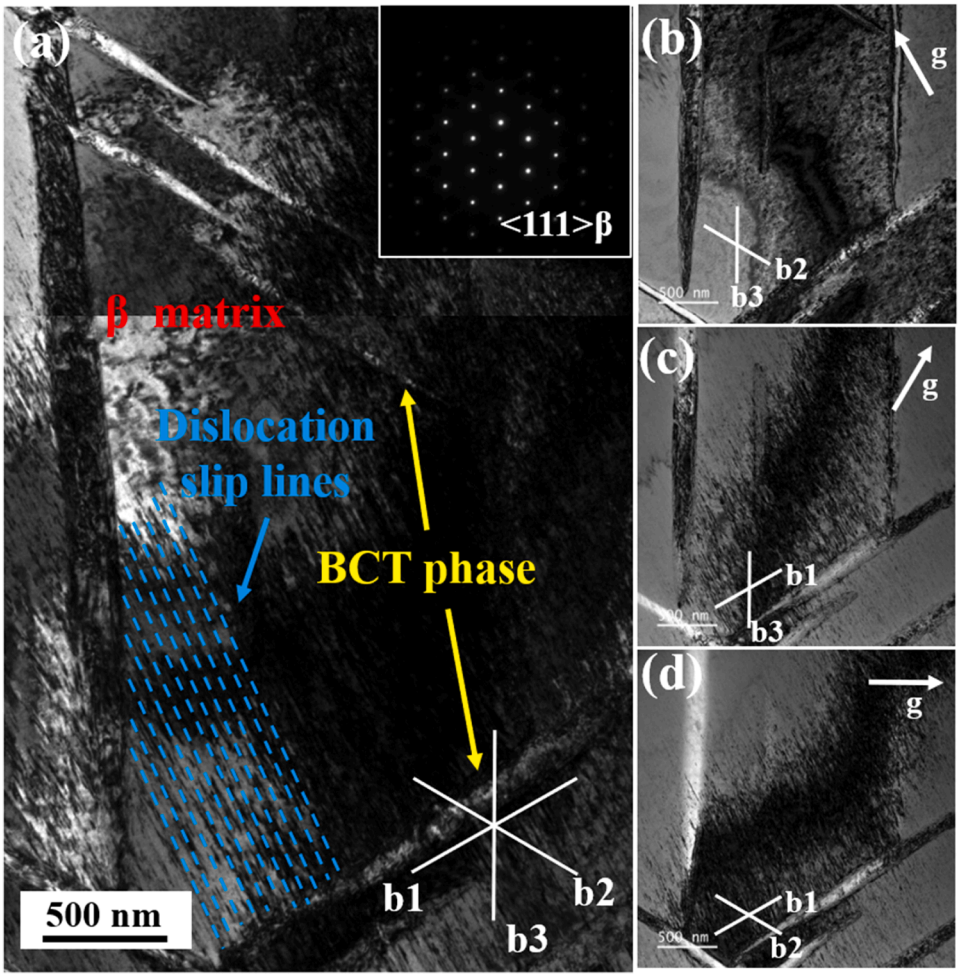

Fig. 10. TEM micrographs of Zr-12Nb-3Sn sample at the early stage of deformation. (a) BF image of dislocation slip lines generated in the β matrix; (b-d) BF images of the three g conditions around $<111>_{\beta}$ zone axis.

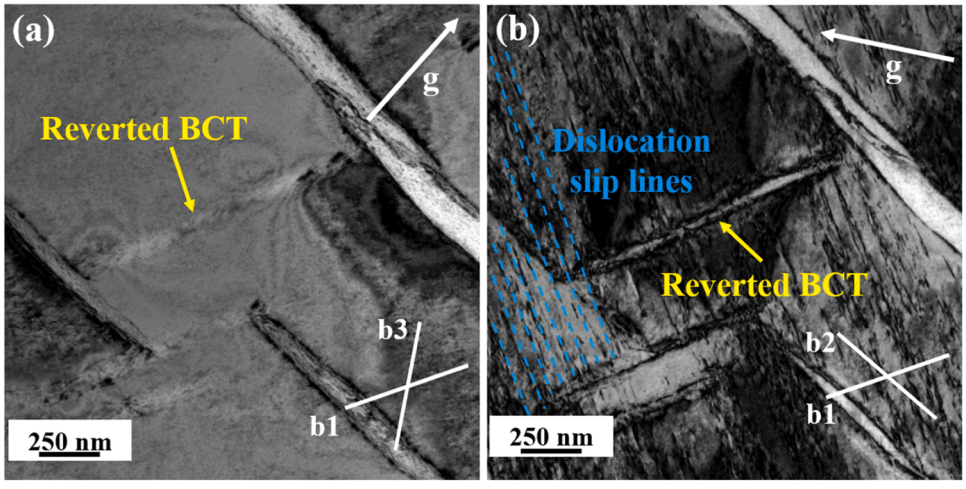

Fig. 11. TEM micrographs of Zr-12Nb-3Sn sample after fracture showing the interaction relationship between dislocation slip lines and BCT phases; (a) and (b) BF images of the g conditions around $<111>_{\beta}$ zone axis.

expansion along the c-axis compared to the BCC matrix. This morphology allows the precipitate surfaces to expand freely, minimizing local shear stresses and lowering overall strain energy compared to other geometries. The reduced strain energy promotes a uniform distribution of precipitates within the matrix, enhancing their ability to hinder dislocation motion. Consequently, plate-like phases are likely to be substantially effective to increase the alloy's yield strength. However, the increasing of the strength usually leads to trade-off with ductility, and even embrittlement [48–50]. Thus, the BCT phases in TWIP Zr offer exceptional advantages because of their stress-dependent reversion

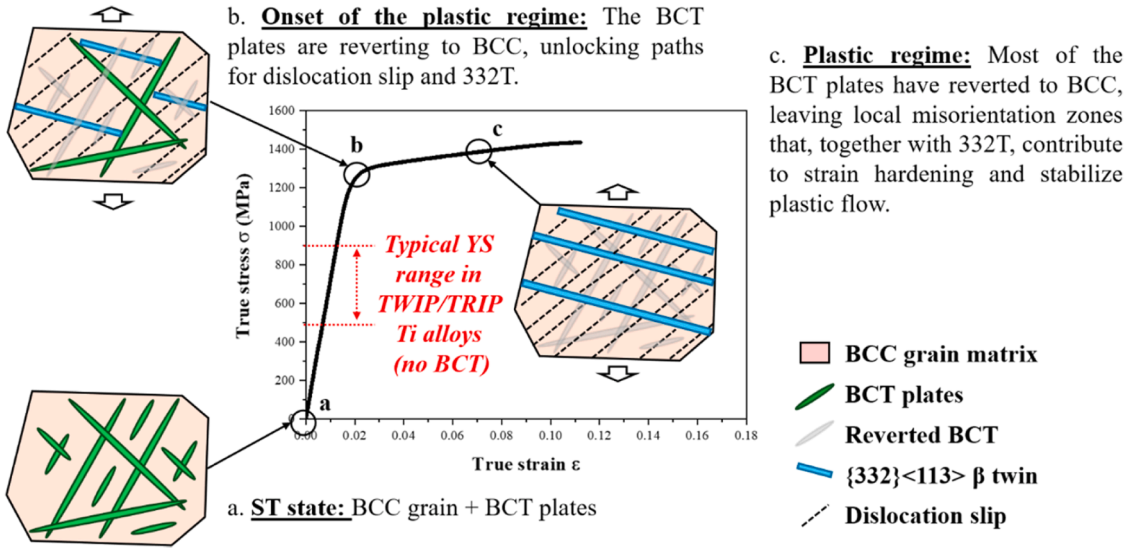

Fig. 12. Schematic illustration of the evolution of the microstructure of the Zr-12Nb-3Sn alloy when deformed in tension. The activation sequence of different deformation mechanisms is shown from the ST state (a) to the different deformation stages (b) onset of the plastic regime and (c) the plastic regime.

behavior, which results in high yield stress without observable embrittlement.

Furthermore, it is noteworthy that in the $\overline{Bo} - \overline{Md}$ design diagram for Zr-based alloys of our previous work [32], the composition of Zr-12Nb-3Sn lies on the TWIP line, indicating that its deformation mechanism is at the threshold for producing the TWIP effect. In our previous studies on dual-phase β Zr-Nb alloys [31], β Zr-Nb-Sn alloys [32] and TRIP/TWIP Ti alloys [28,51], we observed an increase in yield strength when martensitic transformation and 332T were suppressed by enhancing the stability of the β phase.

This provides valuable insight into designing high-strength metastable Zr-based alloys. By leveraging the unique plate-like morphology and reversible transformation behavior of the BCT phase, we propose that tuning the stability of the β phase to a critical level could maximize the strength of the alloy while retaining its deformation capabilities.

6. Conclusions

In summary, the dual-phase Zr-12Nb-3Sn alloy exhibits an exceptional balance of high yield strength and low elastic modulus, largely attributed to the presence and behavior of plate-like BCT phases. A comprehensive suite of microstructural characterizations has been conducted to elucidate the deformation mechanisms and functional role of the BCT phase. The key conclusions are as follows:

(1) The BCT phase forms as three distinct crystallographic variants and exhibits stress-induced transformation into the matrix β phase. This transformation is confirmed by EBSD and TEM analyses, revealing the phase's mechanical instability and reversible nature under load;
(2) The BCT phases act as effective barriers to dislocation motion, contributing to precipitation strengthening. Upon transformation, the reverted BCT continues to impede dislocation slip lines and generates GNDs due to the lattice misfit and ~10% dilatational strain, further enhancing the alloy's strength;
(3) The alloy composition was strategically chosen along the TWIP line to achieve high β phase stability near the mechanical twinning limit. The TWIP effect, observed through the activation of 332T, contributes to a hardening effect during plastic deformation to avoid strain softening.

Overall, the alloy achieves a rare synergy of mechanical properties, with a yield strength exceeding 1200 MPa, an elastic modulus around 70 GPa, and an elongation of about 13%, making it a promising candidate for orthopedic implant applications.

CRediT authorship contribution statement

Junhui Tang: Writing – original draft, Validation, Methodology, Data curation, Conceptualization. **Nicolas Jobit:** Methodology, Data curation. **Agata Sotniczuk:** Writing – review & editing. **Witold Chromiński:** Writing – review & editing, Resources, Methodology, Investigation. **Denis Laillé:** Resources, Methodology. **Daniel Galy:** Writing – review & editing, Software, Methodology, Data curation. **Philippe Vermaut:** Methodology, Investigation, Conceptualization. **Phillippe Castany:** Resources, Methodology, Data curation. **Thierry Gloriant:** Resources. **Ju Li:** Writing – review & editing, Conceptualization. **Frédéric Prima:** Writing – review & editing, Supervision, Conceptualization. **Fan Sun:** Writing – review & editing, Writing – original draft, Validation, Methodology, Investigation, Formal analysis, Data curation, Conceptualization.

Declaration of competing interest

The authors declare that they have no known competing financial interests or personal relationships that could have appeared to influence the work reported in this paper.

Acknowledgements

Fan Sun acknowledges the supports of French Agence Nationale de la Recherche (ANR), under grants ANR-21-CE08-0022 (project ISANAMI) and ANR-24-CE19-7635 (APEX-STENT). Fan Sun acknowledges the support of Global Seed Fund PSL 2023 for visiting scholar at MIT. Junhui TANG is sponsored by China Scholarship Council. The authors would like to thank Sandrine Zanna for her assistance in using the GATAN PECS II MODEL 685 for ion-milling.

References

[1] D.J. Kereiakes, D.A. Cox, J.B. Hermiller, M.G. Midel, W.B. Bachinsky, E.D. Nukta, M.B. Leon, S. Fink, L. Marin, A.J. Lansky, Usefulness of a cobalt chromium coronary stent alloy, Am. J. Cardiol. 92 (4) (2003) 463–466.
[2] A. Mehjabeen, T.T. Song, W. Xu, H.P. Tang, M. Qian, Zirconium alloys for orthopaedic and dental applications, Adv. Eng. Mater. 20 (9) (2018) 1800207.

[3] M. Geetha, A.K. Singh, R. Asokamani, A.K. Gogia, Ti based biomaterials, the ultimate choice for orthopaedic implants – a review, Prog. Mater. Sci. 54 (3) (2009) 397–425.
[4] S.G. Steinemann, Metal implants and surface reactions, Injury 27 (1996) SC–16.
[5] D.R. Sumner, T.M. Turner, R. Igloria, R.M. Urban, J.O. Galante, Functional adaptation and ingrowth of bone vary as a function of hip implant stiffness, J. Biomech. 31 (1998) 909–917.
[6] M. Morinaga, N. Yukawa, T. Maya, K. Sone, H. Adachi, Theoretical design of Titanium alloys, in: Sixth World Conference on Titanium. France; Vol. 1 (1988) p. 1601.
[7] D. Kuroda, M. Niinomi, M. Morinaga, Y. Kato, T. Yashiro, Design and mechanical properties of new β type titanium alloys for implant materials, Mater. Sci. Eng. A. 243 (1998) 244–249.
[8] M. Abdel-Hady, K. Hinoshita, M. Morinaga, General approach to phase stability and elastic properties of β-type Ti-alloys using electronic parameters, Scr. Mater. 55 (2006) 477–480.
[9] M. Marteleur, F. Sun, T. Gloriant, P. Vermaut, P.J. Jacques, F. Prima, On the design of new β-metastable titanium alloys with improved work hardening rate thanks to simultaneous TRIP and TWIP effects, Scr. Mater. 66 (2012) 749–752.
[10] F. Sun, J.Y. Zhang, M. Marteleur, T. Gloriant, P. Vermaut, D. Laille, P. Castany, C. Curfs, P.J. Jacques, F. Prima, Investigation of early stage deformation mechanisms in a metastable β titanium alloy showing combined twinning-induced plasticity and transformation-induced plasticity effects, Acta Mater. 61 (2013) 640606417.
[11] J.Y. Zhang, F. Sun, Z. Chen, Y. Yang, B.L. Shen, J. Li, F. Prima, Strong and ductile beta Ti-18Zr-13Mo alloy with multimodal twinning, Mater. Res. Lett. 7 (2019) 251–257.
[12] X.L. Zhao, M. Niinomi, M. Nakai, T. Ishimoto, T. Nakano, Development of high Zr-containing Ti-based alloys with low Young's modulus for use in removable implants, Mater. Sci. Eng. C. 31 (2011) 1436–1444.
[13] R. Karre, M.K. Niranjan, S.R. Dey, First principles theoretical investigations of low Young's modulus beta Ti-Nb and Ti-Nb-Zr alloys compositions for biomedical applications, Mater. Sci. Eng. C. 50 (2015) 52–58.
[14] Y.L. Hao, S.J. Li, S.Y. Sun, C.Y. Zheng, R. Yang, Elastic deformation behaviour of Ti-24Nb-4Zr-7.9Sn for biomedical applications, Acta Biomater. 3 (2007) 277–286.
[15] Y.L. Hao, M. Niinomi, D. Kuroda, K. Fukunaga, Y.L. Zhou, R. Yang, A. Suzuki, Young's modulus and mechanical properties of Ti-29Nb-13Ta-4.6Zr in relation to α'' martensite, Metal. Mater. Trans. A. 33A (2002) 3137–3144.
[16] M. Long, H.J. Rack, Titanium alloys in total joint replacement-a materials science perspective, Biomaterials 19 (1998) 1621–1639.
[17] M. Niinomi, Mechanical properties of biomedical titanium alloys, Mater. Sci. Eng. A. 243 (1998) 231–236.
[18] P. Laheurte, F. Prima, A. Eberhardt, T. Gloriant, M. Wary, E. Patoor, Mechanical properties of low modulus beta titanium alloys designed from the electronic approach, J. Mech. Behav. Biomed. Mater. 3 (2010) 565–573.
[19] S. Guo, J.M. Zhang, Y. Shang, J.S. Zhang, Q.K. Meng, X.N. Cheng, X.Q. Zhao, A novel metastable β-type Zr-12Nb-4Sn alloy with low Young's modulus and low magnetic susceptibility, J. Alloys Compd. 745 (2018) 234–239.
[20] R. Kondo, N. Nomura, Y.Tsutsumi Suyalatu, H. Doi, T. Hanawa, Microstructure and mechanical properties of as-cast Zr-Nb alloys, Acta. Biomater. 7 (2011) 4278–4284.
[21] R.H. Xue, D. Wang, Y.Y. Tian, J. Wang, L.B. Liu, L.G. Zhang, Zr-xNb-4Sn alloys with low Young's modulus and magnetic susceptibility for biomedical implants, Prog. Nat. Sci. 31 (2021) 772–778.
[22] K.G. Wang, R. Yin, X.N. Xu, W.C. Wei, Y.Y. Tian, Z.X. Deng, L.G. Zhang, L.B. Liu, A study of mechanical and magnetic properties in a metastable Zr-10Nb-6Sn alloy for MRI-compatible hard tissue replacements, J. Mater. Res. Technol. 29 (2024) 2959–2970.
[23] L. Nie, Y.Z. Zhan, T. Hu, X.X. Chen, C.H. Wang, β-Type Zr-Nb-Ti biomedical materials with high plasticity and low modulus for hard tissue replacements, J. Mech. Behav. Biomed. Mater. 29 (2014) 1–6.
[24] Y.N. Zhang, H.L. Yang, A.N. Juaim, X.N. Chen, C. Lu, L. Zou, Y.Z. Wang, X. W. Zhou, Biocompatibility and osteogenic activity of Zr-30Ta and Zr-25Ta-5Ti sintered alloys for dental and orthopedic implants, Trans. Nonferrous Met. Soc. China 33 (2023) 851–864.
[25] C. Leyens, M. Peters, Titanium and Titanium Alloys: Fundamentals and Applications, Wiley-VCH Verlag GmbH & Co. KGaA, Weinheim, FRG, 2003.
[26] B.N. Qian, S.A. Mantri, S. Dasari, J.Y. Zhang, L. Lilensten, F. Sun, P. Vermaut, R. Banerjee, F. Prima, Mechanisms underlying enhanced strength-ductility combinations in TRIP/TWIP Ti-12Mo alloy engineered via isothermal omega precipitation, Acta Mater. 245 (2023) 118619.
[27] L. Lilensten, Y. Danard, R. Poulain, R. Guillou, J.M. Joubert, L. Perriere, P. Vermaut, D. Thiaudiere, F. Prima, From single phase to dual-phase TRIP-TWIP titanium alloys: design approach and properties, Materialia 12 (2020) 100700.
[28] F. Sun, F. Prima, T. Gloriant, High-strength nanostructured Ti-12Mo alloy from ductile metastable beta state precursor, Mater. Sci. Eng. A. 527 (2010) 4262–4269.
[29] F. Sun, J.Y. Zhang, P. Vermaut, D. Choudhuri, T. Alam, S.A. Mantri, P. Svec, T. Gloriant, P.J. Jacques, R. Banerjee, F. Prima, Strengthening strategy for a ductile metastable β-titanium alloy using low-temperature aging, Mater. Res. Lett. 5 (2017) 547–553.
[30] T. Ingale, A. Sharma, J.H. Tang, A. Chesetti, S.K. Sarkar, V. Soni, S.A. Mantri, Y. F. Zheng, F. Sun, N.B. Dahotre, F. Prima, R. Banerjee, Extending strain hardening to high yield strengths in additively manufactured Ti-10V-2Fe-3Al alloy via confined stress-induced transformations, Acta Mater. 298 (2025) 121437.
[31] J.H. Tang, A. Zorgati, J.B. Gaillard, P. Vermaut, F. Prima, F. Sun, Twinning-induced plasticity (TWIP) effect in multi-phase metastable beta Zr-Nb alloys, J. Mater. Sci. Technol. 139 (2023) 120–125.
[32] J.H. Tang, H.T. Yang, B.N. Qian, Y.F. Zheng, P. Vermaut, F. Prima, F. Sun, TWIP-assisted Zr alloys for medical applications: Design strategy, mechanical properties and first biocompatibility assessment, J. Mater. Sci. Technol. 184 (2024) 32–42.
[33] G. Torun, T. Momose, X.H. Sun, W.W. Zhou, K. Kikuchi, N. Nomura, A. Lawasaki, Microstructure and mechanical properties of MRI-compatible Zr-9Nb-3Sn alloy fabricated by a laser powder bed fusion process, Addit. Manuf. 52 (2022) 102647.
[34] W. Tasaki, F. Okabe, Y. Sato, S. Miyazaki, H.Y. Kim, Constituent phases, microstructures, and martensitic transformation of β-type Zr-Nb-Sn alloys, Mater. Sci. Eng. A. 876 (2023) 145121.
[35] EduPack ANSYS Granta, Material Selection: Biomaterials Database, ANSYS Inc., Cambridge, UK, 2024.
[36] M.L. Picklesimer, Oak ridge USA report ORNL-2422, 1957, pp.117.
[37] H.L. Yakel, Oak ridge USA report ORNL-2839, 1959, pp.51.
[38] Y.J. Zhao, M. Rajkowski, Y.L. Gong, S. Laube, L. Perri`ere, A. Kauffmann, J. P. Couzinie, G. Laplanche, T. Li, Role of oxygen in phase stability and mechanical behavior of the bcc HfNbTaTiZr high-entropy alloy during aging, Acta Mater. 298 (2025) 121400.
[39] E. Okunishi, M.Mitsuhara T.Kawai, M.Itakura S.Farjami, M.Nishida T.Hara, HAADF-STEM studies of athermal and isothermal ω-phases in β-Zr alloy, J. Alloys Compd. 577S (2013) S713–S716.
[40] Y. Fu, Y. Gao, W.T. Jiang, W.L. Xiao, X.Q. Zhao, C.L. Ma, A Review of deformation mechanisms, compositional design, and development of titanium alloys with transformation-induced plasticity and twinning-induced plasticity effects, Metals 14 (2024) 1–24.
[41] P.H. Chang, A.G. Preban, The effect of ferrite grain size and martensite volume fraction on the tensile properties of dual phase steel, Acta Metall. 33 (1985) 897–903.
[42] J.D. Eshelby, F.C. Frank, F.R.N. Nabarro, XLI. The equilibrium of linear arrays of dislocations, PhiI. Mag. 42 (1951) 351–364.
[43] Y. Danard, R. Poulain, M. Garcia, R. Guillou, D. Thiaudière, S. Mantri, R. Banerjee, F. Sun, F. Prima, Microstructure design and in-situ investigation of TRIP/TWIP effects in a forged dual-phase Ti-10V-2Fe-3Al alloy, Materialia 8 (2019) 100507.
[44] P. Zhang, S.X. Li, Z.F. Zhang, General relationship between strength and hardness, Mater. Sci. Eng. A. 529 (2011) 62–73.
[45] Y.T. Cheng, C.M. Cheng, Relationships between hardness, elastic modulus, and the work of indentation, Appl. Phys. Lett. 73 (1998) 614–616.
[46] W.C. Oliver, G.M. Pharr, Measurement of hardness and elastic modulus by instrumented indentation: advances in understanding and refinements to methodology, 19 (2004) 3-20.
[47] F.R.N. Nabarro, The strains produced by precipitation in alloys, in: Proceedings of the Royal Society of London. Series A, Math. Phys. Sci. 175, 1940, pp. 519–538.
[48] X.J. Jiang, L.W. Zhang, G.W. Sun, J.H. Yang, Q.X. Ran, H.Y. Wu, Excellent mechanical properties of a Ti-based alloy via optimizing grain boundary α phase, Mater. Lett. 333 (2023) 133662.
[49] P. Yadav, K.K. Saxena, Effect of heat-treatment on microstructure and mechanical properties of Ti alloys: An overview, Mater. Today Proc. 26 (2020) 2546–2557.
[50] J.K. Fan, J.S. Li, H.C. Kou, K. Hua, B. Tang, Y.D. Zhang, Microstructure and mechanical property correlation and property optimization of a near β titanium alloy Ti-7333, J. Alloys Compd. 682 (2016) 517–524.
[51] F. Sun, J.Y. Zhang, C. Brozek, M. Marteleur, M. Veron, E. Rauch, T. Gloriant, P. Vermaut, C. Curfs, P.J. Jacques, F. Prima, The role of stress induced martensite in ductile metastable Beta Ti-alloys showing combined TRIP/TWIP effects, Mater. Today Proc. 2S (2015) S505–S510.